

Chapter 1

Image-Based Closed-Loop Control of Molecular Dynamics: Controlling Strong-Field Dissociative-Ionization Pathways

G.-Y. Chen, J. Lee, H. Jang, D.B. Foote and W.T. Hill III

Abstract In this chapter we will describe a genetic-algorithm search method employing velocity map imaging, 2D fitness functions and multiple search criteria that allow different parts of the control landscape to be examined. We will show how this approach can be exploited for both probing and controlling a rich array of dynamics in polyatomic molecules in a clear and transparent way. As an example of its power and versatility, we will control the bending vibration of CO₂ during dissociative ionization while searching two distinct parts of the control landscape. In so doing, we have tested the theoretical prediction that all solutions are optimal when the constraints are not too severe. Finally, we will show that multiple solutions render the dynamics more transparent, enabling important steps toward deciphering the solution to be made.

G.-Y. Chen

Department of Physics, University of Maryland, College Park, USA
e-mail: gychen@umd.edu

J. Lee · H. Jang

Joint Quantum Institute, University of Maryland, College Park, USA
e-mail: jlee.optics@gmail.com

H. Jang

e-mail: hjang@umd.edu

D.B. Foote

Joint Quantum Institute and Institute for Physical Science and Technology,
University of Maryland, College Park, USA
e-mail: dbfoote@umd.edu

W.T. Hill III(✉)

Department of Physics, Joint Quantum Institute and Institute for Physical
Science and Technology, University of Maryland, College Park, USA
e-mail: wth@umd.edu

1.1 Introduction

Phase and spectrally-shaped laser pulses obtained via a combination of closed-loop feedback and learning algorithms (e.g., genetic or evolutionary algorithms, collectively referred to as GA in this chapter) can be used to produce a so-called optimal control pulse (OCP). These OCPs can be remarkably, if not surprisingly, effective at controlling a quantum system, where it is difficult, if not impossible, to articulate the problem analytically a priori. Given a *suitable* fitness function, however, the system essentially learns what pulse is required to achieve the desired result. In contrast to traditional searches that tend to follow local gradients, GA searches can avoid getting trapped at local maxima. Theoretically, all solutions are optimal solutions if the constraints on the search space are not too severe; there are no suboptimal solutions [1]. Experimentally, obtaining the optimal solution depends strongly on the fitness function. To maximize product yield or any well-defined endpoint that can be measured directly, such as isolating a single harmonic during high-harmonic generation, a scalar usually serves quite well as the fitness function. There are cases of interest, however, where a scalar may not be most appropriate. In experiments employing velocity map images, for example, the most appropriate fitness function will be associated with regions of the image that could be both noncontiguous and two-dimensional (2D). In this chapter we will describe a GA-search method employing velocity map imaging and 2D fitness functions, and use them to study the “no suboptimal solutions” prediction. We will also show that this approach enables a rich array of dynamics to be studied and controlled, some of which are more transparent and less ambiguous than possible by other means.

Our target system, CO₂, has been the subject of strong-field dissociative ionization since the early 1990s, yet it continues to attract attention making it an ideal candidate for adaptive control studies. When exposed to intense near infrared radiation, CO₂ undergoes structural changes, which are partially responsible for the molecule acquiring a relatively large bending amplitude during strong-field dissociative ionization into singly and doubly charged atomic ions [2–6]. The bond length for enhanced ionization has been measured to be about 0.215 nm (4.06 a.u.) [5, 7] while the angular distribution for dissociative ionization is observed to be strongly peaked about the polarization axis obeying $\sim |\cos^{39} \theta|$ [8] for both linear and bent explosions, which corresponds to an alignment parameter of $\langle \cos^2 \theta \rangle \simeq 0.95$. More recent experiments have focused on controlling the strong-field dissociative ionization. For example, Bocharova et al. [7] adjusted the width of an isolated pulse to control ionization and the bond length onset for explosion while Lozovoy et al. [9] and Chen et al. [10] employed adaptive control to find an OCP to enhance the bending vibration. The latter, to our knowledge, was the first image-based closed-loop molecular control demonstration and is the focus in this chapter. A similar approach has recently been used to study larger systems [11].

It is well known that OCPs are generally not unique; typically, more than one solution can be found with nearly the same effectiveness that might be explained by the theoretical prediction mentioned above that the search space can permit multiple solutions in different regions of the search space with none being suboptimal. While

experimental results are consistent with this prediction, to our knowledge this has never been explored systematically experimentally. Such an exploration requires that the same dynamics be controlled via different GA approaches. In [10] we found the OCP with a search-space constraint on what possible OCPs could be created. To test the theoretical prediction, we will present results where we have searched for the OCP using two very different constraints involving different regions of the landscape.

This paper is organized as follows. The experimental setup and approach, including the 2D fitness function, will be described in Sect. 1.2. The experiments performed and their results will be outlined in Sect. 1.3 while their interpretation will be discussed in Sect. 1.4. Finally, we will add a few concluding remarks in Sect. 1.5.

1.2 Experimental Setup and Tools

Figure 1.1 sketches the experimental arrangement used for pulse shaping, strong-field dissociative ionization, GA-mediated landscape searching, and image capture. The experiments were driven by nearly transform limited, linearly polarized pulses produce by a Ti:sapphire laser system (not shown), which was adjusted to yield a kilohertz train of 1 mJ pulses with ~ 15 nm bandwidth. The pulses were shaped with a 128-elements liquid crystal spatial light modulator (CRI SLM-128) capable of phase and amplitude modulation. The spectral bandwidth of the pulse shaper was ~ 25 nm, when centered at 800 nm. After shaping, the beam was divided with a 80/20 beam splitter; the bulk of the energy was used for the experiment while the pulse was characterized with the remainder. The intensity in each arm was controlled independently with an (identical) attenuator composed of a half-wave plate and a polarizer. Pulses sent to the chamber, housing our 4π -image spectrometer [12], were focused with a spherical mirror (f.l. ~ 75 mm) to about a $7.2 \mu\text{m}$ radius, which was sufficient to create dissociative-ionization of CO_2 leading to doubly-charged atomic ions.

Nominally, the pulses were 50 fs in duration (corresponding to a bandwidth of ~ 15 nm) and centered at ~ 800 nm. In the single-pulse control scheme that we employed, the optimal pulse both controlled and assessed the dynamics, the latter via direct Coulomb-explosion imaging [12]. Consequently, we only shaped the phase (and not the amplitude) of the pulse to ensure there was sufficient intensity after shaping to ionize the parent molecular system multiple times, typically requiring an intensity $> 10^{14} \text{ W/cm}^2$. Our experiments were performed with an ambient CO_2 pressure of $\sim 5 \times 10^{-8}$ Torr at laser intensities in the 0.5 to $2.7 \times 10^{15} \text{ W/cm}^2$ range, which was sufficient intensity to remove five or six electrons prior to an energetic dissociation into $\text{O}^{l+} + \text{C}^{m+} + \text{O}^{n+}$ where $l, m, n = 1, 2$ subject to $l + m + n = 5, 6$. We imaged exclusively doubly charged O and C ions by gating the MCP voltage. An MCP gate resolution of 100 ns was sufficient to separate the first three charge states and to exclude protons, OH and N ions. Figure 1.2a is a typical image obtained after about 1 million laser shots. These composite images can be obtained with either the analog or digital camera.

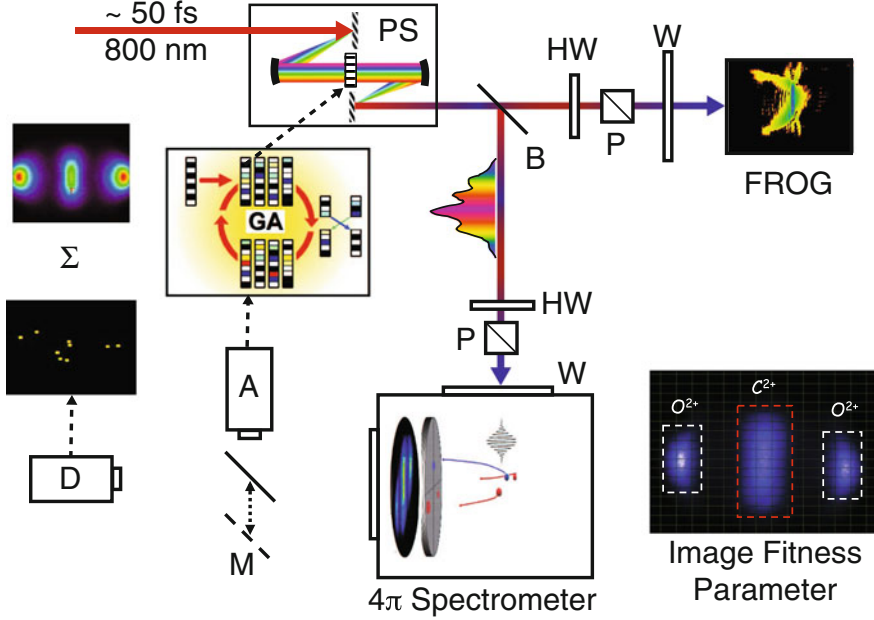


Fig. 1.1 Experimental arrangement for pulse shaping, image capture with our 4π -image spectrometer that uses a micro channel plate (MCP) to detect the ions [12], genetic algorithm feedback loop and pulse characterization using FROG [13]: *PS* spatial light modulator: based pulse shaper; *HW* half-wave plate; *P* polarizer; *W* window; *A* analog CCD camera used for the GA analysis; *D* high frame-rate digital CCD camera used for single-shot image capture and coincidence imaging; and *M* movable mirror to switch between cameras. Also shown are example images (clockwise from *top left*) a composite image, a FROG image of an OCP pulse, regions of the explosion image used as 2D fitness functions and a single frame image corresponding to a single laser shot generating four to six explosion events

1.2.1 Pulse Characterization

Pulses were characterized by transient-grating FROG (frequency-resolved optical gating [13]) running in polarization gating (PG) mode, where the nonlinear medium was a microscope cover slide of thickness ~ 0.2 mm. This characterization included retrieving the intensity and phase versus time and wavelength using standard FROG analysis software [16]. To ensure FROG characterization of the pulse was representative of the beam sent to the experimental chamber, we placed the same optical elements (viewport, beam attenuator, mirrors, etc.) in both arms. The only difference between the beams was that the FROG beam was transmitted through the 80/20 beam splitter while the experimental-chamber beam was reflected. Our tests showed that this did not cause any serious issues with determining the spectral phase.

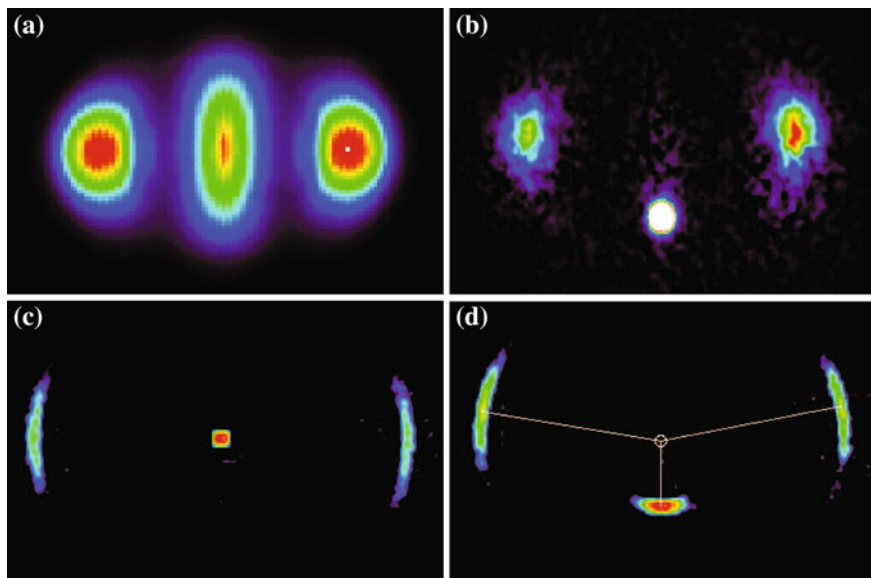


Fig. 1.2 Images of charge distributions of doubly charged ions, O^{2+} (outer lobes) and C^{2+} (central lobe), generated via explosions of CO_2^{n+} ($n = 5, 6$) obtained with the digital camera in Fig. 1.1 with the laser polarization axis horizontal on the page, which is parallel the plane of the MCP: **a** composite image charge distribution containing all doubly-charged trajectories (singly-charged ions not included) and channels (see text) after about 2.5×10^6 laser shots; **b** ions with their trajectories parallel to the MCP corresponding to a symmetric bent explosion of CO_2^{5+} with a specific bond angle extracted from (a) using the selective average techniques described in [14]; **c** triple-coincidence image of the angular distribution about the polarization axis in a plane parallel to the MCP for symmetric linear explosions CO_2^{6+} extracted from (a) using coincidence-imaging techniques (see text), which are described in [15] and references therein; **d** triple-coincidence image of the angular distribution about the polarization axis in a plane parallel to the MCP for symmetric bent explosions at a specific bond angle extracted from (a)

1.2.2 Image Spectrometer

The 4π -image spectrometer, which was inspired by the fast-ion imaging by Kanter et al. [17] and the photoelectron imaging detector of Helm et al. [18], has been described in detail elsewhere [12, 19]. Briefly, it consists of a uniform static electric extraction field (~ 250 V/cm) with an image-quality microchannel plate (MCP) to capture/image the ions created at the focal point. The focal point is located a perpendicular distance from the center of 40 mm dia. MCP circle. In operation, the polarization axis of the light is oriented perpendicularly with respect to the flight path to the MCP and parallel to the surface of the MCP. Atomic ions resulting from the explosions are swept towards the MCP by an extraction electric field. The spectrometer was run in two distinct modes: (i) summed acquisition, which we employed for GA closed-loop searches and (ii) single-shot acquisition, which we employed to analyze the

dynamics. In the summed mode an analog CCD camera was used to capture images of the phosphor screen 640×480 pixel array. The camera frames were streamed to disk at 15 fps where they were summed in real time. The laser was ran at 1 kHz repetition rate so each camera frame contained a sum of ~ 67 laser shots, each of which inducing about 50 explosion events. Suitable images for GA analysis were typically captured within 1–2 min, corresponding to a composite image with a few tens of thousands of explosion events. In the single-shot mode, a fast-frame digital camera (730 fps) was used to capture images of the phosphor screen in 128×128 pixel array, each frame of which corresponding to a single laser shot. These camera frames were synchronized to the repetition rate of the laser, 700 Hz in this case, streamed to disk at 700 fps and stored individually. Figure 1.2a shows a composite image after $\sim 2.5 \times 10^6$ laser shots obtained either from the analog camera or summed images from the digital camera. When the digital camera is used it is possible to extract images in Fig. 1.2b–d as described below. In particular, Fig. 1.2b is associated with explosions that occur in a plane parallel to the detector face at a specific bond angle. Figure 1.2c, d show the angular distribution about the polarization axis for linear and bent explosions taken from [8]. In the bent case it is important to recognize that the bond angle is fixed.

The image in Fig. 1.2a is a 2D representation of a three-dimensional explosion; not all ion trajectories are parallel to the MCP. Consequently, the image is not a representation of the ions' momenta directly because of distortion by out-of-plane trajectories (see [19] for a more complete discussion). An extraction of the momentum distribution, which is necessary to determine the pre-explosion structure and any collateral dynamics (e.g., angular distributions), requires the various trajectories associated with different angles to be deconvolved via one of several possible techniques (see, for example [19–24]).

We used an alternative approach to extract this information from images taken with the digital camera. Each digital frame is associated with one-and-only-one laser shot, which enables correlation analysis—*image labeling* [14, 15], *triple coincidence* [8, 15] and *joint variance* [15]—to be used to select trajectories that were initially ejected in a plane parallel to the surface of the MCP. The images shown in Fig. 1.2 c and d, for example, were obtained from triple coincidence. The (x, y) positions of the ions relative to the center of the image are the true 2D momenta.

Genetic-Algorithm searches require images to be obtained as quickly as possible. One does not want to use any of the deconvolution or post-selection algorithms just mentioned in conjunction with a GA search because they are too slow to be incorporated into a feedback loop. It turns out that GA searches can be performed on raw images. This is possible if (1) specific areas on the image that are concomitant with the dynamics can be identified and (2) these areas can be used as the fitness function. Such areas become the fingerprints of the dynamics we wish to control, as detailed in Sect. 1.2.4. One example is the length of the C^{2+} central lobe in Fig. 1.2a. More acute bending necessarily involves a longer lobe so a fitness function could involve maximizing the lobe length. Once a solution is found, digital images are captured and triple-coincidence is used to quantify the bending.

We end this section by noting that the 4π -image spectrometer is similar to the family of image spectrometers based on recoil ion imaging, *COLTRIMS* (Cold Target Recoil Ion Molecular Spectroscopy) [25–27], which was developed independently at about the same time as ours is perhaps the most familiar.¹ The fundamental difference between the two approaches is in the way the electrons after the MCP are captured. We employ a phosphor screen and a CCD camera to determine the location of electrons ejected by the MCP rather than the position sensitive delay-line array used by *COLTRIMS*. This seemingly small difference has significant consequences. Whereas as the spatial (i.e., energy) resolution in the plane of the MCP is nominally the same for the two approaches, *COLTRIMS* has higher energy (i.e., temporal) resolution in the time-of-flight (TOF) direction, which obviates the need for a deconvolution to determine momentum distributions. Higher resolution in this third dimension, however, comes at the expense of limiting the maximum number of simultaneous hits on the MCP per laser shot. For the standard delay-line detector with four axes (read-outs), *COLTRIMS* is most effective for diatomic systems and about one molecular explosion per shot. The 4π spectrometer, by contrast, is able to handle many tens of simultaneous hits per laser shot and large molecules. Recently, a six-axis delay-line detector was introduced that increases the number of simultaneous hits significantly, enabling *COLTRIMS* to be employed with polyatomic systems as well [28]. The poorer temporal resolution in the TOF direction places limitations on the 4π spectrometer associated with overlapping trajectories (within tens of nanoseconds) and channel saturation (charges from certain channels appearing with each laser shot). The 4π spectrometer, however, has the advantage when it comes to GA searches and closed-loop feedback control. Many thousands of laser shots are required for GA searches because a discernible image of the explosion must be analyzed in realtime during the GA steps, described below, in order to reach convergence. Image capture with *COLTRIMS* is slower, by about an order of magnitude because generally only one molecular explosion per laser shot possible rather than many tens. This makes imaging with cameras more desirable (and cheaper) for GA searches. The 4π and *COLTRIMS* spectrometers are, thus, complementary.

1.2.3 GA Search Approach

Optimal fields obtained via GA searches depend critically on the *fitness function*, a measurable outcome strongly correlated with the desired dynamics (or final state) that the optimal field is to control. As already mentioned, in experimental searches, maximizing the fitness function must be done repeatedly, in real time, and as fast as possible so that the parameter space can be searched quickly. This is extremely

¹While our current application does not include a cold molecular beam it could easily be added. The comparison we make between the two approaches is limited to the detection of the electrons ejected from the MCP, which is used to amplify the ion signal. Thus, we will refer to this family of spectrometers as *COLTRIMS* in this section.

important because depending on the number of *genes*—independent parameters—the search space can be extremely large. For example, there are about 2.5×10^{462} possible settings in our pulse shaper spanning 4π —128 elements each with 12-bit resolution; in this case there would be 128 genes. Things are not quite this bad because the SLM steps are nonlinear. However, even if we only scan over a 2π range, at 800 nm there are still about 1.5×10^{364} possible settings corresponding to about 700 steps between 0 and 2π . Depending on the dynamics, it is sometimes possible to reduce the space further by constraining the search as we discuss in Sect. 1.3. These constraints must be added carefully so as not to exclude the optimal solutions. Consequently knowledge of the dynamics and the systems is essential to run a GA successfully. As mentioned above, we use an area on the images as the fitness function, which falls into the class of 2D fitness functions. Two-dimensional fitness functions provide more detailed control of a specific channel while also allowing multiples channels to be controlled simultaneously. To control specific channels and dynamics, we must have an image *fingerprint* that identifies the desired process. We will discuss fingerprinting in the next section.

Our GA searches followed the traditional approach outlined in [29], with each of our generations consisting of 40 individuals. The population of each successive generation was obtained via fitness-proportional selection, recombination (one-point crossover), mutation, elitism and replacement. In fitness-proportional selection, the probability of an individual to have offsprings is proportional to its fitness. In one-point crossover, the genes of a chosen pair of individuals selected randomly are swapped. In mutation, every gene is given a chance, typically small but can be varied during the search, for its value to be altered by an amount chosen randomly. By piling up several mutations, a gene can migrate far away from initial value. The elitism operation passes a certain number of copies of fittest individual to the next generation to ensure that it will not be lost. Finally, individuals not satisfying a minimum intensity requirement to produce ionization are eliminated from the gene pool; the eliminated genes are replaced by others randomly generated and commensurate with the specific GA operation stage.

1.2.4 Channel Fingerprinting

Channel fingerprinting involves associating explosion channels with unique areas on the image. To that end, we simulated the three-body explosion by solving the coupled equations of motion,

$$m_i \ddot{r}_i = -\frac{e^2}{4\pi\epsilon_0} \frac{\partial}{\partial r_i} \sum_{j \neq i}^N \frac{q_i q_j}{R_{ij}}, \quad (1.1)$$

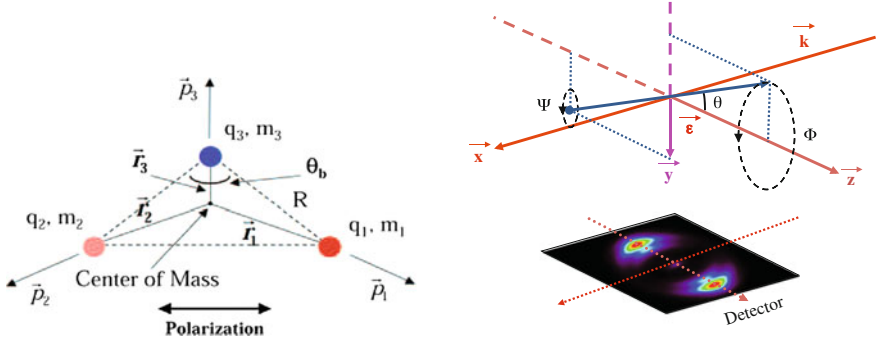


Fig. 1.3 Molecular geometry at the time of the explosion (*left*) and explosion geometry relative to the detector. *Left* q_i and m_i are the number of elemental charges, e ($q_i e$ is the charge of mass m_i), and the masses respectively, \vec{r}_i and \vec{p}_i are the distances from the center of mass and the initial momenta respectively, R are the charge separations (i.e., $R_{ij} = |\vec{r}_i - \vec{r}_j|$ and θ_b is the bond angle. *Right* $\vec{\epsilon}$ and \vec{k} are the polarization axis (parallel to \vec{z}) and the propagation vector (parallel to \vec{x}) respectively, θ is the angle between the dipole moment of the molecule and $\vec{\epsilon}$, Φ the azimuthal angle the dipole moment of the molecule makes with $\vec{\epsilon}$ and Ψ is the rotation of the molecule around its dipole moment (clearly only important when the molecule is bent

subject to the classical hamiltonian,

$$H = \sum_{i=1}^N \frac{1}{2} m_i \dot{\vec{r}}_i^2 + \frac{e^2}{4\pi\epsilon_0} \sum_{i>j}^N \frac{q_i q_j}{R_{ij}}, \quad (1.2)$$

for a pure Coulomb explosion. In (1.1) and (1.2), R_{ij} are the critical radii (R_c s) for enhanced ionization [30, 31], ϵ_0 is the vacuum permittivity and the rest of the parameters are defined in Fig. 1.3. For the three-atom (CO₂) explosion of interest, $N = 3$. In principle, one could partially account for residual bonding in a mean field way by including a charge defect (σ), where $q \rightarrow q_{eff} = q - \sigma$ [5]. The Coulomb approximation near R_c is pretty good when five or six electrons are removed, however, so we did not use an effective charge in our simulations.

We modeled the dissociative ionization for the three channels that populate our images—(222), (221/122) and (212). The simulations were run in four steps, consistent with the recent experimental observation of Bocharova et al. [7]. Step one was the removal of three electrons from the parent CO₂. Step two was an expansion of the system to R_c .² Step three was the removal of two or three additional electrons (via enhanced ionization) creating CO₂⁵⁺ or CO₂⁶⁺. Step four was the Coulomb explosion from R_c into the atomic ions. One generally observes a range of bond lengths centered about R_c in experiments, which could be due to a combination of issues such as molecules in the most intense part of the beam being ionized before R_c , motion

²Bocharova et al. [7] found that CO₂³⁺ is the intermediate state enabling the system to reach R_c and supporting the ensuing dynamics, not CO₂²⁺ suggested by theory [6, 32].

during ionization and potential curves not being purely Coulombic. Bocharova et al. [7] found CO_2 takes about 100 fs to reach R_c , which they report to be about 0.21 nm. Zhao et al. using 100 fs pulses found an R_c of about 0.24 nm. Thus, to accommodate these variations, we allowed the CO bond lengths to be distributed with a bi-Gaussian distribution about the measured R_c of [5]. Specifically, for lengths shorter than R_c the width of the Gaussian was chosen to be $0.2(R_c - R_e)$, where R_e is the equilibrium CO bond length for neutral ground state CO_2 . For lengths longer than R_c , the width was set to $0.5(R_c - R_e)$. These choices were commensurate with the spreads observed by Chen et al. [10]. In the simulation, the two bond lengths were selected randomly and weighted by the half Gaussians independently, allowing for the possibility of one bond being longer than the other. We assumed that the probability for ionization was governed by the angle of the time-averaged dipole moment of CO_2 . For linear CO_2 the angular distribution for linear and bent explosions was measured to be $\propto \cos^n \theta$, with n being ~ 39 [8], where θ is the angle between the dipole moment of the molecule and the polarization axis of the laser. (The absolute value of a normalized distribution produces an alignment parameter, $\langle \cos^2 \theta \rangle$, for dissociative ionization of ~ 0.95 .)

A simulated image of the explosion was prepared by summing a large number of simulated explosion events with CO_2^{+m+n+} randomly oriented (i.e., random values for θ , Ψ and Φ) consistent with the above constraints. Image generation had two components—Coulomb repulsion and field extraction. The atomic ions ($\text{O}^{+} + \text{C}^{m+} + \text{O}^{n+}$) were allowed to expand under their mutual Coulomb force for about 5 ps at which time the Coulomb force was turned off because beyond this time it had negligible affect on the final momenta of the ions. At the same time, the ions were subjected to a static electric field pushing them toward the detector. Knowing the strength of the field and the distance to the detector, it was possible to determine where each ion will land on the MCP. This Monte Carlo simulation granted us the ability to relate the molecular dynamics to the contours of the image, thus identifying areas to be used as fitness functions for GA control—channel fingerprints, if you will. For symmetric bending of the (222) channel, the length of the central C^{2+} lobe corresponding to ions that have no momentum along the polarization axis is ideally suited as the fingerprint. This fingerprint shown in Fig. 1.4d; the associated fitness function for enhancing the bending amplitude corresponds to maximizing the length of this area. The response with and without running the GA search is shown in the two triple-coincidence images in Fig. 1.5. It is evident that both the C^{2+} lobe and the O^{2+} arc lengths are longer for the GA pulse. We point out that areas on the image where C^{2+} have momentum along the polarization axis identify an asymmetric explosion channel where either the CO bond lengths or the O ion charges are unequal. The hyperbolic area in Fig. 1.4a shows an appropriate fingerprint for such asymmetric explosions. In conjunction with the (222)-channel fingerprint, depending on the separation of the vertices, this hyperbolic fingerprint can be used to isolate the (221)/(122) channels from the (222) channel. Maximizing the relative strengths of one over the other allows the relative strength of these two

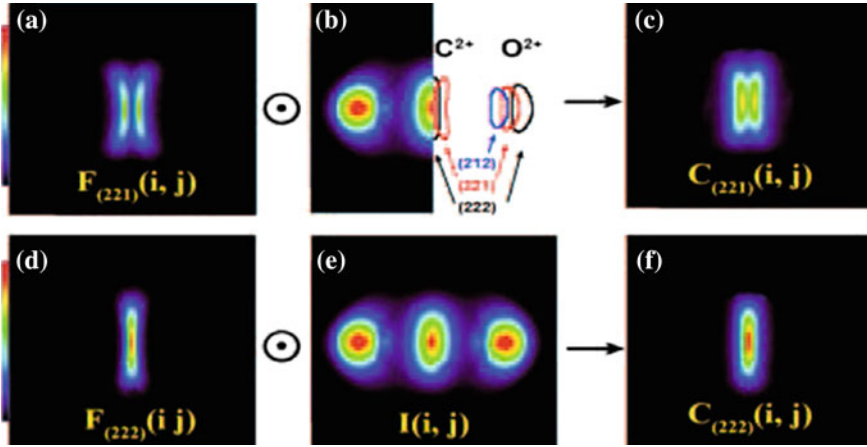


Fig. 1.4 Channel *fingerprints*, determined by simulations and represented as outlines in *panel b*, used as channel masks to enable area fitness functions for the (212), (221) and (222) channels. *Panel e* is a composite image of the doubly charged ions, $I(i, j)$, and *panel b* is an overlay of the fingerprints on $I(i, j)$. The isolated C^{2+} distributions associated with the channel masks shown respectively for simulated spectra ($F_{(221)}(i, j)$ and $F_{(222)}(i, j)$) and experimental spectra ($C_{(221)}(i, j)$ and $C_{(222)}(i, j)$). We do not isolate the (221) and (122) channels so $F_{(221)}(i, j)$ and $C_{(221)}(i, j)$ represent both channels

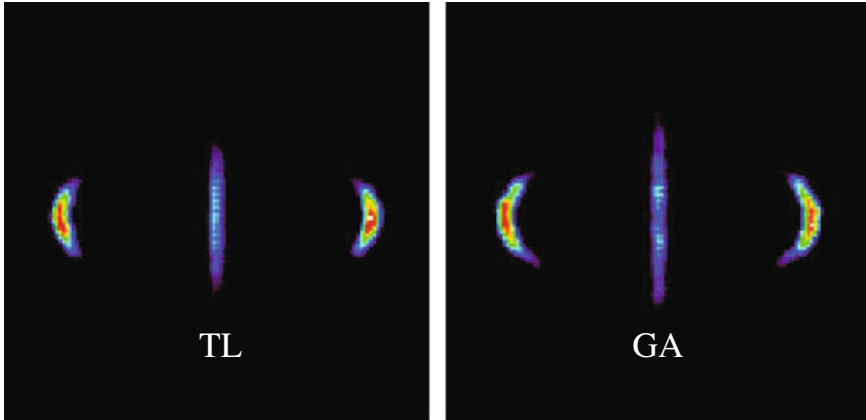


Fig. 1.5 Two triple-coincidence explosion images induced by TL (*left*) and GA-solution pulses. The TL image was obtained at an intensity of about $7 \times 10^{14} \text{ W/cm}^2$ and the GA was obtained with the last peak in the train equivalent to about $6 \times 10^{14} \text{ W/cm}^2$

channels to be controlled [33]. Using just one leg of the hyperbola enables isolation of the (221) from the (122) channel. In the remainder of this chapter we will focus on the (222) channel. The other channels will be treated in a separate publication.

1.3 GA Control of CO₂ Bending Amplitude

We will now present the results of three sets of experiments associated with enhancing the bending vibration amplitude of the (222) channel. Two sets of GA searches were run with two different fitness functions. We also ran control experiments with a single pulse that was either transform limited or chirped (in the positive or negative sense). It is commonly believed that the large number of possible settings associated with pulse shaper, $\sim 1.5 \times 10^{364}$ in our case, contains a high degree of redundancy. Consequently, to expedite finding optimal solutions, investigators have looked for ways to reduced the size of the search space. This is particularly true for complicated searches where convergence is an issue. This tends to be less of a concern for simple searches such as creating a transform limited pulse using the strength of the second harmonic signal as the fitness function. For our GA search for an OCP, we found that unless the space was reduced, the search did not converge. Reducing the space, however, must be done judiciously so as not to exclude the optimal solution from the space. Here, we present results where the space was reduced in two ways. The first, which was presented in [10], exploited the dynamics of the problem to reduce the number of genes from 128 to 4, leading to a search space of about 2.4×10^{11} possibilities. We will refer to this as the restricted search. In the second GA search we relaxed the restrictions of the first considerably and searched a space with about 4×10^{41} possible settings. We will refer to the second as the unrestricted search as it is thirty orders of magnitude larger than the first. The second experiment was done for two reasons: (1) to verify that the restricted OCP was part of the unrestricted space and (2) to test the no suboptimal solution hypothesis.

In [10] we showed that it is possible to choose a set of genes that reflects the nature of the dynamics we were trying to control. Specifically, we demanded that the solutions searched induce periodic kicks to the molecule. This was motivated by the idea that if we repeatedly hit the molecule at the right frequency with the right phase we could enhance the bending just like pushing a child on a swing. The basis set had just four genes that were related to terms in a 5th-order Taylor expansion of the spectral phase,

$$\varphi(\omega) = \sum_{n=0}^5 \varphi_n(\omega_0) \frac{(\omega - \omega_0)^n}{n!}, \quad (1.3)$$

where $\varphi_n(\omega_0) \equiv \partial^n \varphi(\omega) / \partial \omega^n|_{\omega_0}$. While φ_0 and φ_1 determined the envelope phase and group delay, and thus are ignored in our search, the remaining four produced a train of pulses that are chirped and composed of peaks with increasing intensity. The left column of Fig. 1.6 shows two solutions that we will refer to as the *restricted* solutions. The traces are FROG reconstructions of the temporal intensities (black curves) and phases of the pulses.

In the second GA experiment we allowed the pixels to change independently. However, we did add two restrictions to eliminate some of the possible settings. First, we locked four adjacent pixels together, reducing the number of independent spectral units to 32; each pixel in a four-pixel unit was set to the same value during

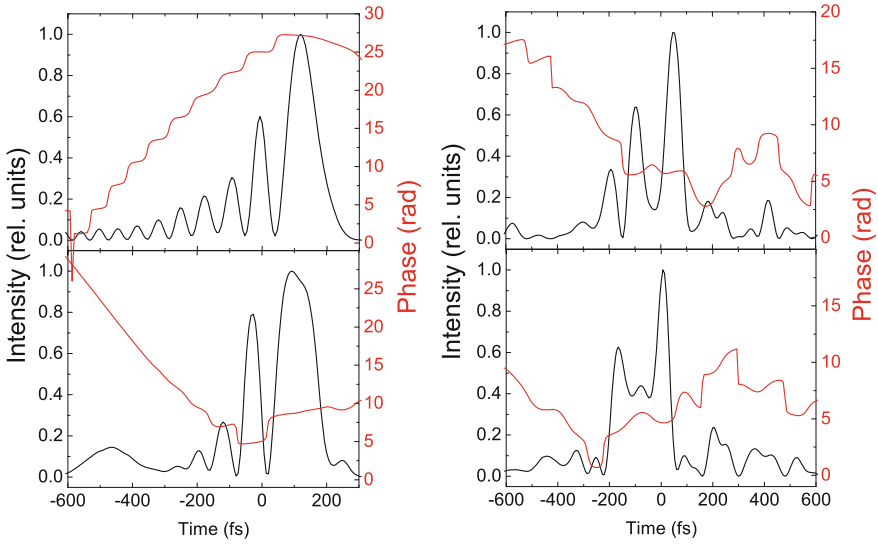


Fig. 1.6 Two *restricted*-GA solutions (FROG reconstructions) obtained with the Taylor-expansion gene set (*left*) and two *unrestricted*-GA solutions obtained with the 32-member gene set and a Gaussian cost functional. The *black* curves are the temporal intensities (*left axis*) and the *red* curves are the temporal phases (*right*)

the search. We also reduced the number of phase steps to 20; a four-pixel unit was allowed to make changes in increments of $\pm\pi/10$.³ Even with only 20 steps, the phase can change drastically from generation to generation so we imposed an impedance to retard how quickly the phase for a particular unit can evolve. Specifically, we limited the range over which the phase of a given four-pixel unit could change in one generation to fall within $\pm\delta$ by adding a Gaussian (with a FWHM = δ) cost functional centered at the current value of φ as shown graphically in Fig. 1.7; small changes are more probable than large changes. The GA solutions found were obtained with $\delta \sim \pi/4$. Two solutions are shown in the right column of Fig. 1.6.

As mentioned in Sect. 1.2.2 once an OCP is found, we exploit triple-coincidence images (similar to those of Fig. 1.5) to determine the bond length distribution. We extract the far-field angles associated with the bending of the molecule from these images. The molecular bond angle, θ_b , defined in the inset of Fig. 1.8, is determined numerically by solving the equations of motion (1.1) and (1.2) as described by Chen et al. [10]. The θ_b values are then plotted as shown in Fig. 1.8. We characterize the magnitude of the bending by the parameter $\Delta_{1/2}\theta_b$, the HWHM of the bending

³The number of steps was chosen to ensure the searches would converge in a reasonable amount of time. We did not explore the sensitivity of the OCP to the number of pixels in a unit nor the number of steps between 0 and 2π .

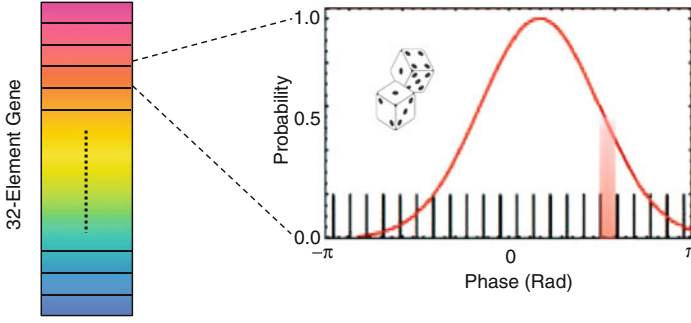
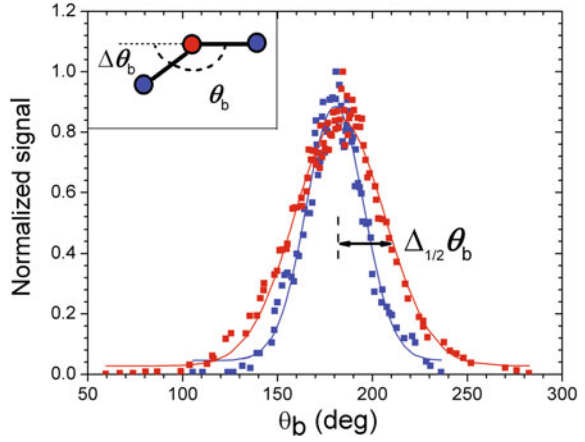


Fig. 1.7 The 20-step phase mutation range modified by a Gaussian cost functional. *Note* The Gaussian width (FWHM = δ , see text) is not to scale

Fig. 1.8 Bond angle distributions obtained from triple-coincidence images as described in [10]. The *red dots* are the bond angle distribution of the optimal pulse taken with the OCP shown in the lower right panel of Fig. 1.6 and the *blue dots* are those of a 50 fs TL pulse. The *solid curves* are Gaussian fits to the data. The *inset* defines the angles



distribution in Fig. 1.8. We compare values of $\Delta_{1/2}\theta_b$ for the two GA and control experiments in Fig. 1.9. This figure is consistent with Fig. 3 of [10] where the GA value for $\Delta_{1/2}\theta_b$ is plotted at an effective intensity, which is determined by a TL pulse with a pulse width and pulse energy equivalent to that of the last peak in the GA solution. Both the width and effective energy of the GA peak are determined by FROG reconstruction. We then compare the bending due to the GA pulse to that of a TL that has a pulse energy equivalent to the total pulse energy of the entire GA pulse. For these experiments, the total pulse energy of the GA pulses was about 50 μJ . A 50 μJ TL pulse corresponds to a TL pulse with an intensity of about $9.4 \times 10^{14} \text{ W/cm}^2$, which is the second TL pulse from the left in Fig. 1.9. The effective intensities for the GA pulses are given in Table 1.1. The two restricted solutions from [10] are also included in this plot.

Fig. 1.9 Bond angle distributions for all four OCPs, 50 fs TL pulses as a function of intensity, and chirped pulses as a function of intensity

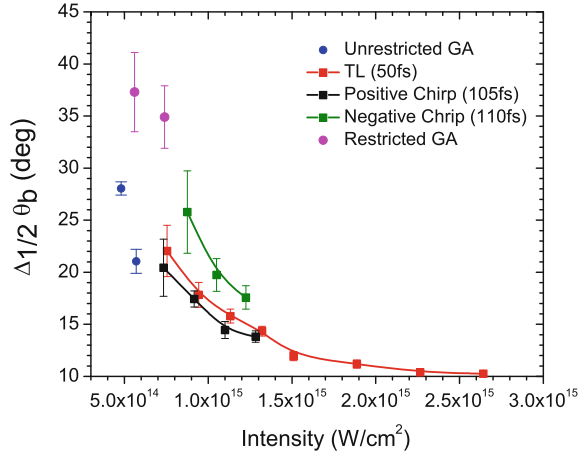


Table 1.1 Pulse parameters and bending results for the restricted ([10]) and unrestricted GA solutions

	A (upper)		A (lower)		B (upper)		B (lower)	
Peak #	1	2	1	2	1	2	1	2
τ_i	100	47	128	52	54	43	52	NA
I_i	7.5	4.2	5.6	4.3	5.7	3.4	4.8	3.2
Δt_{ij}	130		139		144		159	
$\Delta_{1/2}\theta_b$	35°		38°		21°		28°	
% Change	46 %		56 %		19 %		57 %	

A (B) corresponds to the restricted (unrestricted) solution in the left (right) column of Fig. 1.6; peak # 1 (2) corresponds to the last (second to last) peak in the solution pulse trains; τ_i (fs) are the temporal width of the peaks; Δt_{ij} (fs) are the time interval between the last two primary peaks; I_i are the intensity of the peaks in units of 10^{14} W/cm²; $\Delta_{1/2}\theta_b$ is the bending parameter (see text) with an uncertainty of $\pm 1^\circ$ to 2° ; and % change is the enhancement given by $100 \times (\Delta_{1/2}\theta_{b-GA} - \Delta_{1/2}\theta_{b-TL})/\Delta_{1/2}\theta_{b-TL}$ as described in the text

1.4 Discussion

Before we discuss the effectiveness of the GA solutions (OCPs) achieving their goals, we will first compare the structure of the GA solutions. We first note that all four solutions are composed of a set of well-defined peaks. For the restricted GA solution, the train of pulses was a result of an alternation in even and odd orders of a spectral phase [34]. The fact that we see a series of peaks for the unrestricted GA search, lends credence to our initial thought that the OCP should contain periodic kicks by a train of pulses. However, clearly a long train is not necessary because the solutions are not identical. Neither the pulse widths nor their separations are the same. The number of pulses varies drastically from solution to solution and even the phase structure is distinct for each pulse. What does seem to be critical is that the last peak in the chain contain considerably more energy resulting in higher intensity. We showed in [10]

that reversing this trend, by putting the most intense peak first, greatly reduces the enhancement. Clearly, because we can reach a solution with as few as two peaks, a train, albeit short, is required.

1.4.1 GA-Solution for Bending Enhancement

We will now look at the degree to which the GA solutions enhanced the bending. We begin by summarizing the two restricted results. In [10] we determined the effectiveness by comparing $\Delta_{1/2}\theta_b$ produced by GA pulses to that produced by TL pulses with the same width as the last peak in the chain of the GA solution and the same total peak energy. For the restricted solutions, the widths of the last peak varied in duration from 100 to 128 fs (see Table 1.1). Transform-limited pulses of those widths, not shown in Fig. 1.9, produced $\Delta_{1/2}\theta_b \sim 24^\circ$ while the best GA pulse produced $\Delta_{1/2}\theta_b \sim 37.5^\circ$ for a maximum enhancement of $\sim 56\%$.⁴ The other GA solution enhanced the bending by about 46 %. Compared with the TL pulse plotted at an intensity of 9.4×10^{14} W/cm², the two unrestricted GA solutions enjoyed enhancements of 19 and 57 %. We note that the uncertainties in $\Delta_{1/2}\theta_b$ are in the $\pm 1^\circ$ to 2° range.

It is evident that the pulse intensity, pulse width, and the spacing between the last two pulses tend to play a role in enhancing CO₂ bending during dissociative ionization for the symmetric (222) channel. As discussed in [10] bending is inversely proportional to pulse intensity (energy) as shown in Fig. 1.9. Long pulses were shown to lead to more enhancement than shorter. Both of these observations are likely caused by the molecule spending more time in the di- or tri-cation states, with contours that are sensitive to the intensity of the laser (see [6, 32]), before enhanced ionization occurs. The longer pulses give the system more time to respond to the changing shape of the potential surfaces [7]. Figure 1.9 also shows bending is sensitive to the pulse chirp. Negative chirp enhances bending for a pulse with the same width and intensity whereas a positive chirp seems to play a much less critical role. This is due to the curvature of potential surfaces enabling resonance to be maintained longer for negative chirps, which has been observed in other systems as well [35].

Focusing more directly on the GA (OCP) solutions (see Table 1.1 and Fig. 1.9), we notice some of the same trends. Bending is again inversely proportional to intensity. It scales with the duration of the final peak. This is obvious when comparing the restricted solution against the unrestricted solution. The width of the restricted, which is at least twice as large as the unrestricted, are much more effective at enhancing the bending. A similar case can be made between the two unrestricted solutions. While the widths are nominally the same, there is a side peak between the last two major peaks that effectively lengthens the last peak and could contribute to it being

⁴To generate the longer pulses we placed a positive chirped on the pulse. Figure 1.9 shows that a positive chirp does not enhance bending.

a bit more effective. The spacing between the two final peaks is another clue to the control. In our searches, we found more enhancement when the separation was close to an integer multiple of 50 fs, the bending vibrational period of the ground state of CO₂; the restricted solutions are both closer to 150 fs than the unrestricted solutions and the lower unrestricted solution is closer than the upper solution in Fig. 1.7.

It is also important to consider the chirp of the final peaks. In general, when the phase is flat across a peak it is nominally unchirped (transform limited). When the phase is parabolic across the peak with the vertex up (down) it will be positively (negatively) chirped. For the restricted-GA solutions, the upper solution in Fig. 1.7 is more positively chirped than the lower while the lower solution enhances the bending more. The same is true for the unrestricted-GA solution, but in this case the difference between the two is more stark. It is important to note that the difference between their relative effectiveness is also more pronounced than the restricted case. This is consistent with what we observed with a single, negatively-chirped pulse.

1.4.2 Suboptimal Solutions

As the last topic of this chapter we return to the no suboptimal solution prediction. Is it consistent with our experimental observations? Upon first glance it would appear no, because the four GA solutions (OCPs) did not achieve the same degree of bending as measured by $\Delta_{1/2}\theta_b$, which ranges from 21° to 28° for the unrestricted search and 35° to 37.5° for the restricted search. Taking into account the error bars, the restricted solutions are consistent with each other but the unrestricted are on the fringe of agreement at best. There is still the issue, however, the two searches do not achieve the same level of efficiency. Things do not look any better if the percentage enhancement is used as a measure—a range of 46 to 56 % for the restricted solutions and 19 to 57 % for the unrestricted. The error bars are larger but we end up with the same conclusion. To drive this point home, we also found solutions, i.e., GA search converged maximizing the fitness function, but bending was not enhanced. These observations begs two questions: (1) why does it appear there are suboptimal solutions, (2) why does the restricted search do better than the unrestricted?

Taking the second question first, we remind the reader that the restricted search was designed specifically to give the molecule a period kick, which evidently is close to the right solution. While the fitness function asked the search to maximize its length, most (but not all) solutions also maximized the bending. The unrestricted was just that and had to search the landscape for regions to stretch. We suspect that stretching the C²⁺ lobe could be done in ways inaccessible to the restricted search. To backup this conjecture, we created triple-coincidence images selecting parts of the C²⁺ lobe where the C²⁺ had some momentum along the polarization axis using both the restricted and unrestricted solutions. As mentioned in Sect. 1.2.4, these images will pick out asymmetric explosions. While these images only contain

doubly charged ions, the atomic ions can come from both CO_2^{6+} and CO_2^{5+} explosions will. Hence, the C^{2+} and O^{2+} resulting from a GA search can be due to (122), (212), (221) or (222) channels. We discovered that the image associated with the restricted-GA searches had considerably less contamination from CO_2^{5+} explosions than did the images associated with the unrestricted-GA searches. Whereas the C^{2+} arc length resulting from restricted-GA searches was due mostly to the (222) channel those from unrestricted-GA searches had a high degree of contamination from the asymmetric channels, especially (221) and (122). Even though the (222) channel populated both searches, the relationship between the length of the C^{2+} central lobe and the O^{2+} arc length was less isomorphic. That is, the C^{2+} could be extended because of the asymmetric channels without the (222) channel bending more. This is because of the extended focal volume allowing explosions occurring at the edge of the focal volume to produce ions that end up along the central C^{2+} lobe within the fingerprint. These ions will have some momentum along the polarization axis and thus represent asymmetric explosions. These ions come primarily from CO_2^{5+} explosions. The details will be discussed in more detail in a future publication. Suffice it to say, the net result is that the unrestricted searches can maximize the central lobe in ways that do not require the (222) channel to be involved giving solutions the appear to be suboptimal. This seems to occur much less frequently on the restricted landscape.

Returning to the first question, our evidence is consistent with the no suboptimal prediction. We asked the GA to maximize the length of the C^{2+} lobe. When the search converged on a solution it tends to be rather consistent. While this prediction needs to be studied more systematically, we do not disagree with it. What our observations do point out is that for complicated GA searches, more sophisticated fingerprints and fitness functions are required. The 2D approach suggested in this chapter are ideally suited for that purpose.

1.5 Conclusion

In this chapter we have presented a closed-loop GA search approach based on 2D fitness functions. This approach provides much more access to complicated dynamics associated with polyatomic systems than is possible with scalar fitness functions. We showed that careful fingerprinting of channels associated with the dynamics under study is required both to reveal the underlying physics and to control the dynamics upon which it is based. For bending during strong-field dissociative ionization of CO_2 , we were able to link the effectiveness of its control to four distinct parameters that are summarized in Table 1.2. When the GA search converged, it maximized the fitness function, however, the fitness function was only a necessary condition for maximizing bending. As a result, other dynamics contributed to maximizing the fitness function making the suboptimal prediction appear to be violated. To circumvent

Table 1.2 Summary of CO₂ bending responses to pulse parameters during dissociative ionization

Parameters	Bending response
Intensity	Inversely proportional but nonlinear
Width	Directly proportional over the range tested, 50–150 fs
Separation	Larger response near an integer multiple of 50 fs
Chirp	Larger response for negative chirp

this problem, one needs to design more complete fitness function, which is possible with the addition of secondary and tertiary search conditions—areas on the image. To go to the next level, a fingerprint leading to a fitness function that is both necessary and sufficient must be incorporated in the GA search, where the fitness function and the dynamics under study are isomorphic.

Acknowledgments We thank Dr. G.M. Menkir for helpful discussions and technical support in the early stages of this work and Mr. B. Crist for technical support with the simulations. This work was supported by NSF Grant No. PHY0902221.

References

1. H.A. Rabitz, M.M. Hsieh, C.M. Rosenthal, *Science* **303**(5666), 1998 (2004)
2. C. Cornaggia, M. Schmidt, D. Normand, *J. Phys. B: At. Mol. Opt. Phys.* **27**, L123 (1994)
3. C. Cornaggia, F. Salin, C.L. Blanc, *J. Phys. B: At. Mol. Opt. Phys.* **29**, L749 (1996)
4. A. Hishikawa, A. Iwamae, K. Yamanouchi, *J. Chem. Phys.* **111**, 8871 (1999)
5. K. Zhao, G. Zhang, W.T. Hill III, *Phys. Rev. A* **68**, 063408 (2003)
6. Y. Sato, H. Kono, S. Koseki, Y. Fujimura, *J. Am. Chem. Soc.* **125**, 8019 (2003)
7. I. Bocharova, R. Karimi, E.F. Penka, J.P. Brichta, P. Lassonde, X. Fu, J.C. Kieffer, A.D. Bandrauk, I. Litvinyuk, J. Sanderson, F. Légaré, *Phys. Rev. Lett.* **107**, 063201 (2011)
8. K. Zhao, W.T. Hill III, *Phys. Rev. A* **71**, 013412 (2005)
9. V.V. Lozovoy, X. Zhu, T. Gunaratne, D. Harris, J. Shane, M. Dantus, *J. Phys. Chem. A* **112**, 3789 (2008)
10. G.Y. Chen, Z.W. Wang, W.T. Hill III, *Phys. Rev. A* **79**, R011401(R) (2009)
11. E. Wells, C.E. Rallis, M. Zohrabi, R. Siemering, B. Jochim, P.R. Andrews, U. Ablikim, B. Gaire, S. De, K.D. Carnes, B. Bergues, R. de Vivie-Riedle, M.F. Kling, I. Ben-Itzhak, *Nat. Commun.* **4**, 2895 (2013)
12. J. Zhu, W.T. Hill III, *J. Opt. Soc. Am. B* **14**, 2212 (1997)
13. R. Trebino, *Frequency-Resolved Optical Gating: The Measurement of Ultrashort Laser Pulses* (Kluwer Academic Publishers, Boston, 2000)
14. K. Zhao, G. Zhang, W.T. Hill III, *Opt. Express* **9**, 42 (2001)
15. W.T. Hill III, K. Zhao, L.N. Elbertson, G.M. Menkir, in *Progress in Ultrafast Intense Laser Science I*, ed. by K. Yamanouchi, S.L. Chin, P. Agostini, G. Ferrante (Springer-Verlag, Berlin, 2006), Springer Series in Chemical Physics, pp. 59 – 75
16. (2014). URL <http://www.swamptics.com/>
17. E.P. Kanter, P.J. Cooney, D.S. Gemmell, K.O. Groeneveld, W.J. Pietsch, A.J. Ratkowski, Z. Vager, B.J. Zabransky, *Phys. Rev. A* **20**(3), 834 (1979)
18. H. Helm, N. Bjerre, M.J. Dyer, D.L. Huestis, M. Saeed, *Phys. Rev. Lett.* **70**(21), 3221 (1993)

19. K. Zhao, T. Colvin, W.T. Hill III, G. Zhang, *Rev. Sci. Instrum.* **73**, 3044 (2002)
20. C. Bordas, F. Paulig, H. Helm, D. Huestis, *Rev. Sci. Instrum.* **67**, 2257 (1996)
21. G.A. Garcia, L. Nahon, I. Powis, *Rev. Sci. Instrum.* **75**, 4989 (2004)
22. G.M. Roberts, J.L. Nixon, J. Lecointre, E. Wrede, J.R.R. Verlet, *Rev. Sci. Instrum.* **80**, 053104 (2009)
23. E. Wells, J. McKenna, A.M. Sayler, B. Jochim, N. Gregerson, R. Averin, M. Zohrabi, K.D. Carnes, I. Ben-Itzhak, *J. Phys. B: At. Mol. Opt. Phys.* **43**, 015101 (2010)
24. T. Gerber, Y. Liu, G. Knopp, P. Hemberger, A. Bodi, P. Radi, Y. Sych, *Rev. Sci. Instrum.* **84**, 033101 (2013)
25. J. Ullrich, R. Moshhammer, R. Dörner, O. Jagutzki, V. Mergel, H. Schmidt-Böcking, L. Spielberger, *J. Phys. B: At. Mol. Opt. Phys.* **30**, 2917 (1997)
26. R. Dörner, V. Mergel, O. Jagutzki, L. Spielberger, J. Ullrich, R. Moshhammer, H. Schmidt-Böcking, *Phys. Rep.* **330**, 95 (2000)
27. J. Ullrich, R. Moshhammer, A. Dorn, R. Dörner, L.P.H. Schmidt, H. Schmidt-öcking, *Rep. Prog. Phys.* **66**, 1463 (2003)
28. M. Pitzer, M. Kunitski, A.S. Johnson, T. Jahnke, H. Sann, F. Sturm, L.P.H. Schmidt, H. Schmidt-Böcking, R. Dörner, J. Stohner, J. Kiedrowski, M. Reggeline, S. Marquardt, A. Schießer, R. Berger, M.S. Schöffler, *Science* **341**, 1096 (2013)
29. K. Sastry, D. Goldberg, G. Kendall, in *Search Methodologies: Introductory Tutorials in Optimization and Decision Support Techniques*, ed. by E. Burke, G. Kendall, Business Media, LLC (Springer Science, 233 Spring Street, New York, NY 10013, 2005), Chap. 4:, pp. 97–125
30. S. Chelkowski, A.D. Bandrauk, *J. Phys. B: At. Mol. Opt. Phys.* **28** (1995)
31. H. Yu, A.D. Bandrauk, *Phys. Rev. A* **56**, 685 (1997)
32. H. Kono, Y. Sato, M. Kanno, K. Nakai, T. Kato, *Bull. Chem. Soc. Jpn.* **79**, 196 (2006)
33. G.Y. Chen, H. Jang, J. Lee, W.T. Hill III, To be published (2014)
34. K. O’Keeffe, T. Robinson, S.M. Hooker, *J. Opt.* **12**, 015201 (2010)
35. N. Schirmel, N. Reusch, P. Horsch, K.M. Weitzel, *Faraday Discuss.* **163**, 461 (2013)

Progress in Ultrafast Intense Laser Science XII

Yamanouchi, K.; Roso, L.; Li, R.; Mathur, D.; Normand, D.
(Eds.)

2015, XIII, 206 p., Hardcover

ISBN: 978-3-319-23656-8